Fermi level tuning and double-dome superconductivity in the kagome metals $CsV_3Sb_{5-x}Sn_x$

Yuzki M. Oey,[1] Brenden R. Ortiz,[1] Farnaz Kaboudvand,[1] Jonathan Frassineti,[2,3] Erick Garcia,[2]
Rong Cong,[2] Samuele Sanna,[3] Vesna F. Mitrović,[2] Ram Seshadri,[1] and Stephen D. Wilson[1]

[1]*Materials Department, Materials Research Laboratory, and California NanoSystems Institute*
*University of California Santa Barbara, California 93106 United States**
[2]*Department of Physics, Brown University, Providence, RI 02912, U.S.A.*
[3]*Department of Physics and Astronomy "A. Righi", University of Bologna, I-40127 Bologna, Italy*
(Dated: March 4, 2022)

METHODS

Elemental Cs (liquid, Alfa 99.98%), V (powder, Sigma 99.9%), Sb (shot, Alfa 99.999%), and Sn (shot, Alfa 99.9999%). Stoichiometric quantities were weighed in an argon glove box with oxygen and water levels of < 0.5 ppm. Vanadium powder was cleaned prior to the synthesis using EtOH and concentrated HCl to remove residual oxides. Elements were loaded in a tungsten carbide ball mill vial and milled for 60 min in a SPEX 8000D high-energy ball mill. Resulting powders were ground in agate, sieved through a 106 micron sieve, sealed in fused silica, and annealed at 823 K for 48 K. A secondary grind and anneal (723 K, 12 h) was utilized to ensure best superconducting fractions and Sn homogenity. The resulting powder is dark grey and air stable.

High–resolution synchrotron powder X–ray data were acquired at Argonne National Laboratory (APS, 11-BM) with an average wavelength of $\lambda = 0.458$ Å. Powders were diluted with ground silica before packing in 0.8 mm kapton capillaries to reduce X-ray absorption. Additional powder X–ray (pXRD) data were collected on a Panalytical Empyrean powder diffractometer equipped with a PIXcel 1D detector. Topas Academic[1] was used to refine the patterns with Pawley and Rietveld fitting,[2] and crystal structures were visualized using VESTA.[3] A Hitachi TM4000Plus scanning electron microscope (SEM) was used to perform energy–dispersive X–ray spectroscopy (EDS). The AztecOne software was used to analyze and obtain the chemical composition in higher Sn content samples.

A Quantum Design Magnetic Property Measurement System (MPMS) with a vibrating sample magnetometer (VSM) was used to take magnetization data. Approximately 15 mg of powder was packed in a plastic VSM capsule and loaded in a brass rod sample holder. Superconductivity measurements utilized an applied field of 5 Oe. Due to the intrinsically low moment of CsV_3Sb_5, temperature–depeneded CDW measurements utilized a higher field of $H = 10000$ Oe. A Quantum Design Physical Property Measurement System (PPMS) Dynacool was used for resistivity measurements. Resistivity measurements were performed using a standard 4-point contact geometry. Silver paint and gold wire were used to make electrical contact to sintered, pressed bars of CsV_3Sb_5.

The electrical transport option was used with a constant frequency of ∼15 Hz and a current of 1 mA.

The room temperature ^{121}Sb zero field nuclear quadrupolar resonance (NQR) measurements were done at Brown University. The NQR data was recorded using a state-of-the-art laboratory-made NMR spectrometer. The spectra were obtained, at each given value of frequency, from Fourier transforms of the spin-echo. We used a standard spin echo sequence ($\pi/2 - \tau - \pi$). A $\pi/2$ pulse that optimized signal intensity of 3.4 μs was used. The shape of the spectra presented in the manuscript are independent of the duration of time interval τ. The NQR relaxation rate T_1^{-1} was measured using a Spin Stimulated Echo 3-pulse sequence ($\pi/2 - \tau - \pi/2 - \tau_d - \pi/2$) to obtain magnetization recovery curves $M(\tau_d)$. The resulting value of the rate was obtained by fitting the magnetization to a single exponential function of time $M(\tau_d) \propto \exp(-t/T_1)$. Since the nuclear spin I of ^{121}Sb equals to $5/2$ and both Sb sites (Sb1 and Sb2) are in noncubic environments, two distinct quadrupolar lines are observed per site [4]. The shift was obtained from the frequency of the first moment of spectral distribution.

For electronic state calculations, first-principles calculations based on density functional theory (DFT) within the Vienna ab initio Simulation Package (VASP) were performed.[5, 6] The projector augmented wave (PAW) method[7, 8] was employed and relaxations of the ionic positions were conducted using an energy cutoff of 520 eV. Reciprocal space k-point meshes were automatically generated at a density of 55 Å–1 along each reciprocal lattice vector. The band structure was calculated across the main paths along the high symmetry points as defined by Setyawan and Curtarolo.[9] Density of states (DOS) and band structures were visualized using the sumo package.[10] The CsV_3Sb_5 structure has 5 sites for Sb atoms. Two sites are unique and symmetrically distinct: within the kagome plane (WKP), and out of the kagome plane (OKP). In this study we calculated both cases of when Sn is WKP and when Sn is in one of the OKP sites.
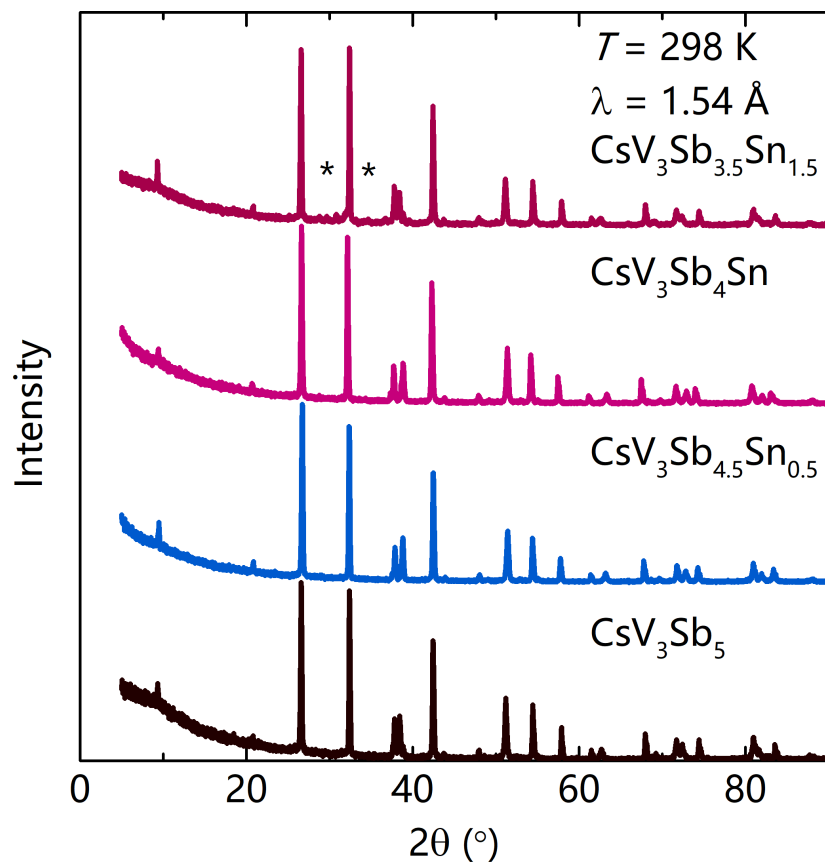
SFIG 1. Powder X–ray diffraction on samples of $CsV_3Sb_{5-x}Sn_x$ for $x = 0$, 0.5, 1.0, and 1.5. Compositions of $x \leq 1$ show single phase samples. A small secondary phase appears for $x = 1.5$, as indicated by the asterisks (*).
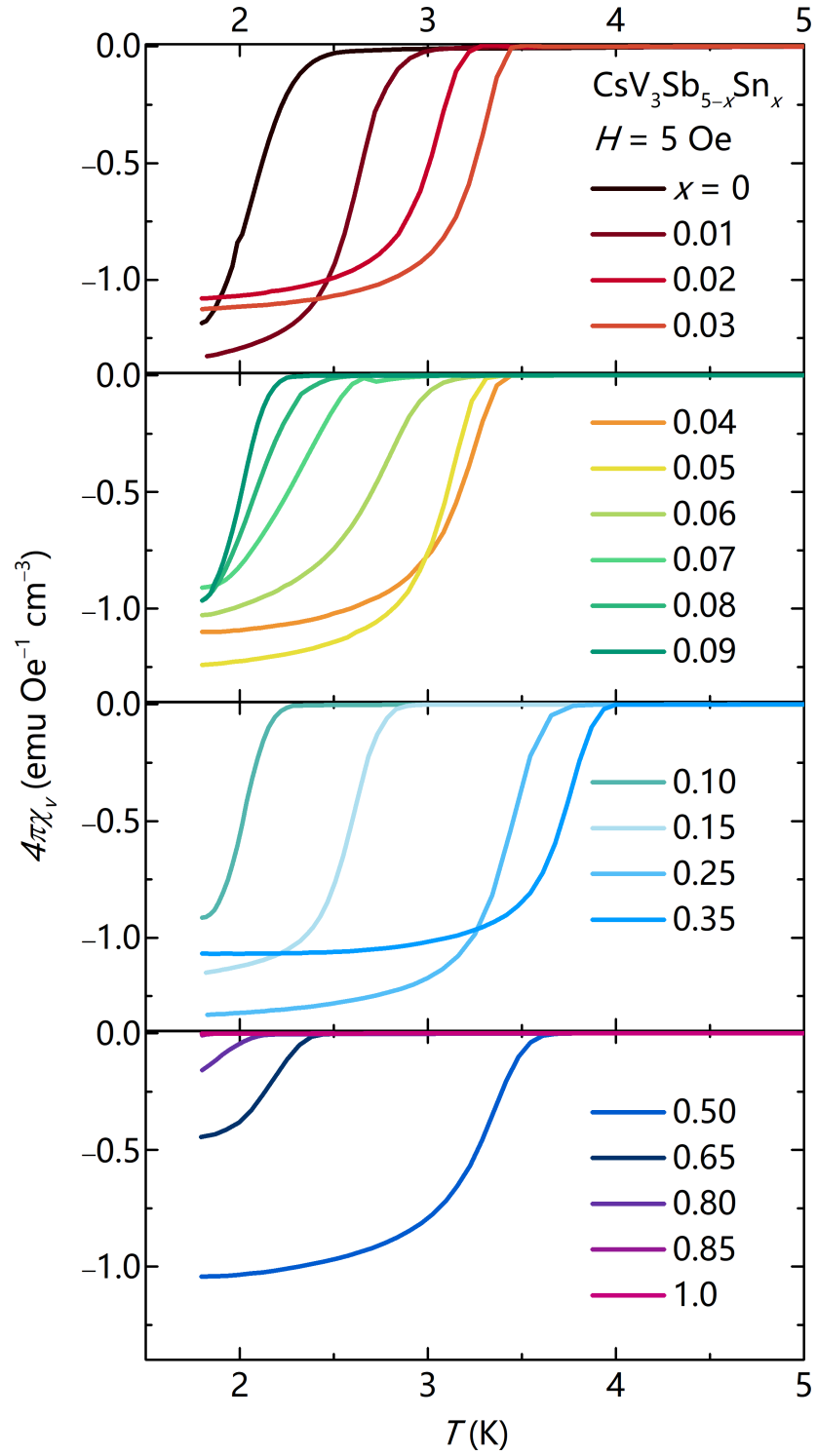
SFIG 2. Susceptibility measurements ($H = 5\,\mathrm{Oe}$) on powders of $CsV_3Sb_{5-x}Sn_x$ for $0 \leq x \leq 1.0$ show that the superconducting fractions, calculated as $4\pi\chi_v$, are ≈ 1 for $x \leq 0.50$. From $x \geq 0.65$, the superconducting fraction decreases, and superconductivity is fully suppressed by $x = 1$.
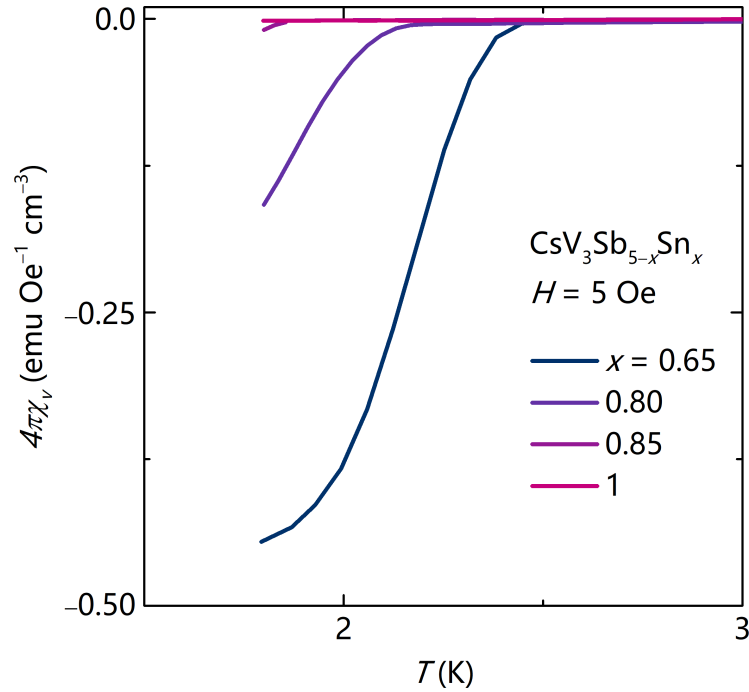
SFIG 3. Susceptibility measurements on powders of $CsV_3Sb_{5-x}Sn_x$ for $x \geq 0.65$ show that the superconducting fraction significantly diminishes. By $x = 1$, there is no trace of superconductivity at 1.8 K. However, it is not clear whether the superconductivity is being suppressed with the higher amounts of Sn doping or if the T_C is below 1.8 K.
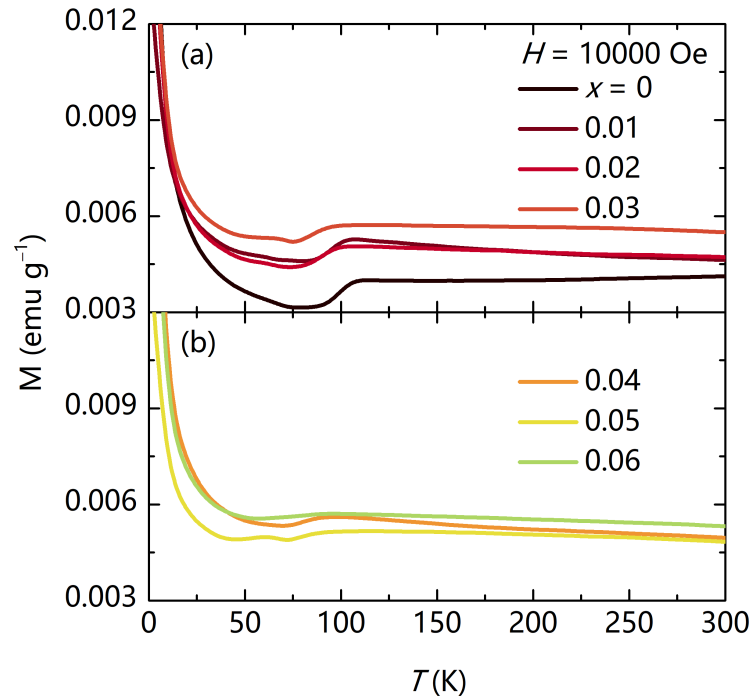
SFIG 4. Magnetization measurements on powders of $CsV_3Sb_{5-x}Sn_x$ ($H = 10000$ Oe) show the suppression of the CDW order by $x = 0.06$. For visual clarity, the datasets are split. Although there is a clear inflection point for $0 \leq x \leq 0.04$, the magnitude of the CDW order significantly decreases and T^* shifts to lower temperature. The additional inflection for $x = 0.05$ at around 55 K can be attributed to oxygen contamination in the chamber of the instrument.
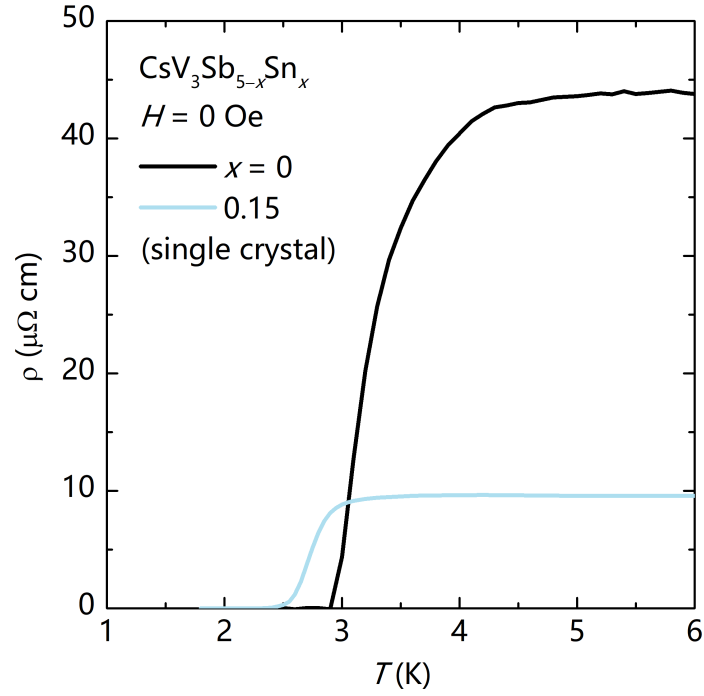
SFIG 5. Resistivity data on single crystal $CsV_3Sb_{4.85}Sn_{0.15}$ complements powder resistivity data in the main text and shows no broadening in the superconducting transition.
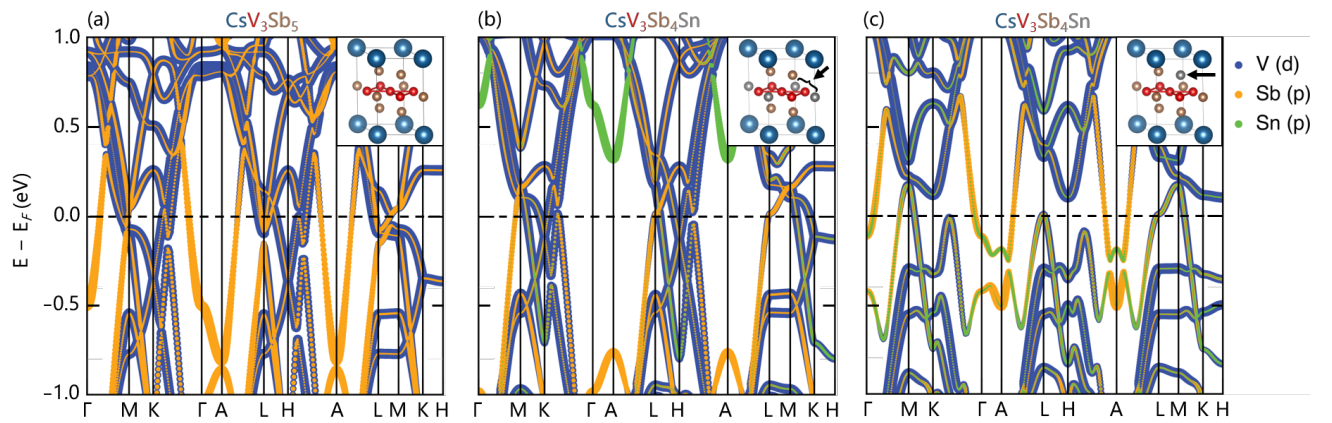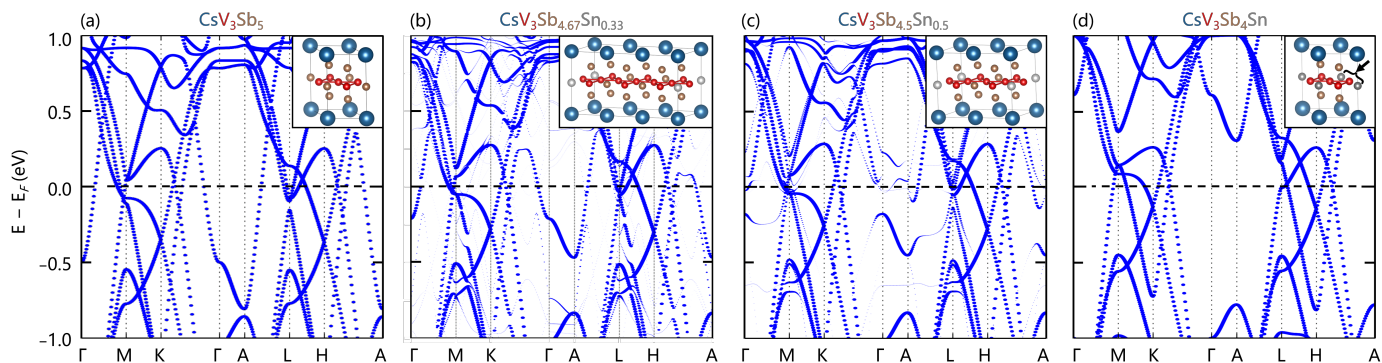

SFIG 6. Colorized bands from DFT calculations show the orbital contributions from V, Sb, and Sn. (a) The Γ pocket in CsV_3Sb_5 is from the Sb p_z orbitals. (b) However, the fully substituted structure with Sn in the kagome plane arises from the Sn p_z orbitals.

SFIG 7. Supercell DFT calculations for $x = 0.33$ and 0.5 show the evolution of bands as Sn content is increased. The Γ pocket lifts through E_F by $x = 0.5$ while the van Hove singularity at the M point crosses E_F by $x = 1$.
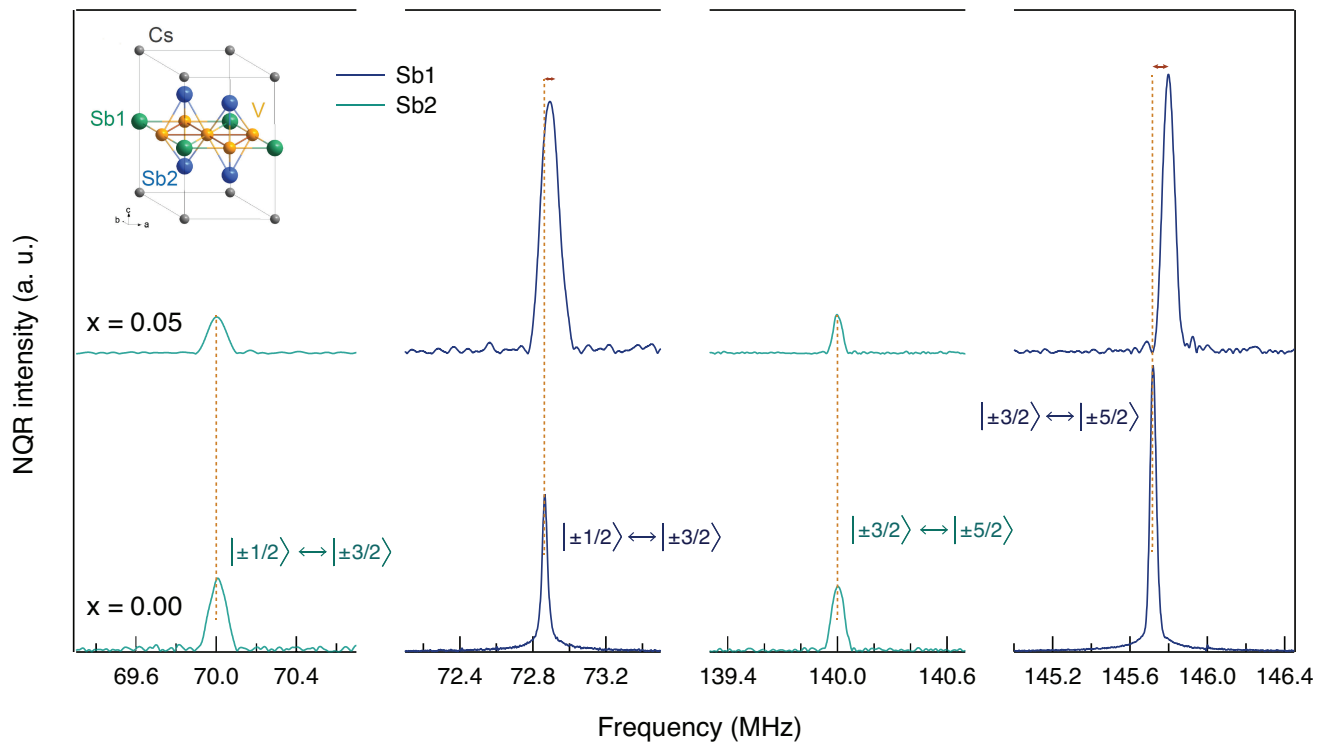
SFIG 8. Sn doping dependence of the NQR spectra for two different Sn concentrations, as denoted. Dashed lines denote position of all the spectral lines of undoped sample. Sb site assignment is depicted in the inset.
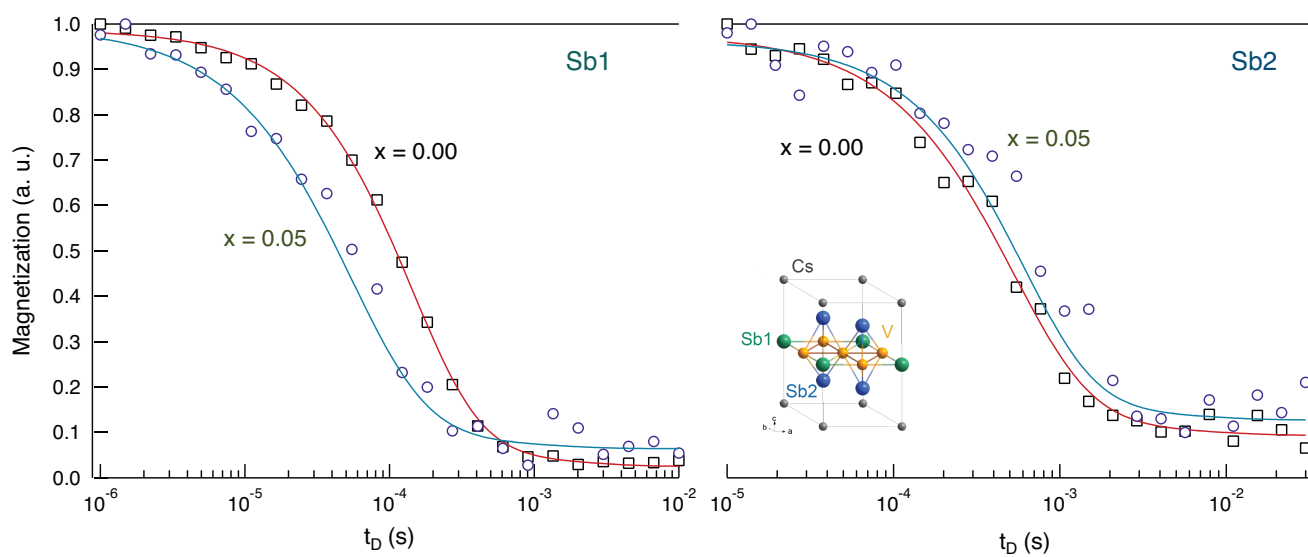
SFIG 9. Nuclear magnetization recovery curves following $\pi/2$ pulse excitation for two Sn doping concentrations, $x = 0$ and $x = 0.05$, for two Sb sites. Sb site assignment is depicted in the inset. Solid lines are fits to the exponential function used to deduce the NMR rate T_1^{-1}.

Sb site	Sn concentration	ν_Q (MHz)
Sb1	0.00	140.0024 ± 0.0012
Sb1	0.05	139.9963 ± 0.0012
Sb2	0.00	145.7197 ± 0.0012
Sb2	0.05	145.7988 ± 0.0012

TABLE I. Doping dependence of the frequency shift of the quadrupolar line for $|\pm 5/2\rangle \leftrightarrow |\pm 3/2\rangle$ transition, for both Sb sites, at room temperature.

Sb site	Sn concentration	T_1 (ms)
Sb1	0.00	6.23 ± 0.44
Sb1	0.05	6.24 ± 0.49
Sb2	0.00	1.87 ± 0.05
Sb2	0.05	1.63 ± 0.09

TABLE II. Relaxation time T_1 for Sb1 and Sb2 sites for two different Sn doping concentrations.

Supplementary Note 1: ^{121}Sb NQR Spectra and Shift

In Supplementary Figure S8 we plot the doping dependence of the NQR frequency spectra for ^{121}Sb sites 1 and 2. In addition, in Supplementary Table SI, we summarize the frequency shift associated with the first moment of Sb site 1 and 2 for two Sn doping concentrations. Evidently, only the Sb2 site line shifts when Sn dopants are added to the sample, while the Sb1 spectra remain at a fixed frequency position, unaffected by Sn doping. Naively, one could conclude that this observation implies that NQR measurements indicate that Sn dopants only occupy Sb2 sites. However, taking into careful consideration the crystalline structure shown in Supplementary Figure S8 and the distances between different Sb sites, we conclude that the observed shift in the quadrupolar frequency of Sb2 sites, can only be accounted for if a low concentration of the Sn dopants replace the in-plane Kagome Sb1 sites.

Specifically, the distances between the Sb1-Sb1 sites are much larger than that between the Sb1-Sb2 ones. Therefore, a substitution of Sn into Sb1 nuclear sites will only affect Sb2 nuclei, since Sb2 nuclei experience a more drastically modified electronic charge distribution, *i.e.* the Electric Field Gradient (EFG) tensor, around them, resulting in a different observed quadrupolar coupling. In the other case, a dopant in Sb2 sites would affect both Sb1 and Sb2 sites, since Sb1-Sb2 and Sb2-Sb2 distances are comparable. If this was the case, an appreciable shift of the quadrupolar frequency should also have been observed for Sb1 sites.

Supplementary Note 2: ^{121}Sb NQR Relaxation Rate

In the absence of magnetic correlation, the NMR relaxation rate is given by

$$\frac{1}{T_1} \propto \int d\varepsilon \, N_\uparrow(\varepsilon) N_\downarrow(\varepsilon) f(\varepsilon)[1 - f(\varepsilon)], \qquad (1)$$

where $N_\downarrow$ and $N_\uparrow$ denote the densities of up- and down-spin states and $f(\varepsilon)$ is the Fermi occupation function. That is, $(T_1)^{-1}$ is proportional to the square of the DOS integrated over energy ε in the range of the order of $k_B T$ around E_F selected by the Fermi function. In Supplementary Figure S9 we plot the magnetization recovery curves used to deduce the relaxation rate for both Sb sites. The values of the rate are summarized in Supplementary Table II. For the Sb1 site the relaxation rate is independent on Sn concentration, within the error bars. However, the Sb2 relaxation rate varies as a function of doping. The above equation implies that the $(T_1)^{-1}$ is proportional to the square of the DOS at the Fermi level. A comparison of the $(T_1)^{-1}$ for the two concentrations at the Sb2 site indicate that the DOS in the $x = 0.05$ sam-

ple increased by 5.5% compared to that in the undoped $x = 0.0$ sample.

Supplementary Note 3: Quadrupolar effects

In the simplest case of zero field NQR, the interaction between eq, the electric field gradient (EFG), and the nucleus, with spin I and the quadrupole moment Q, is described by the Quadrupole Hamiltonian,

$$\mathcal{H}_{Q} = \frac{(eQ)(eq)}{4I(2I-1)}[3I_z^2 - I(I+1)]. \tag{2}$$

For nuclear spin $I = 5/2$, as is the case of ^{121}Sb, the energy eigenstates of $\mathcal{H}_{Q}$ are given by,

$$E = \frac{(eQ)(eq)}{4I(2I-1)}[3m^2 - I(I+1)] \tag{3}$$

The quadrupole Hamiltonian expressed in the coordinate system defined by the principal axes of the EFG, is given by,

$$\mathcal{H}_{Q}(x,y) = \frac{eQV_{zz}}{4I(2I-1)}\left[(3\hat{I}_z^2 - \hat{I}^2) + \eta(\hat{I}_x^2 - \hat{I}_y^2)\right], \tag{4}$$

where $\eta \equiv |V_{xx} - V_{yy}|/V_{zz}$ is the asymmetry parameter and V_{xx}, V_{yy}, and V_{zz} are the diagonal components of the EFG. Here, V_{zz} is defined as the principle component of the EFG and $|V_{xx}| < |V_{yy}| < |V_{zz}|$, by convention.

From [4], for $I = 5/2$ and for an asymmetry parameter $\eta = 0$, there are two lines corresponding to the transitions $|3/2\rangle \to |1/2\rangle$ and $|5/2\rangle \to |3/2\rangle$, given by

$$\nu'_{5/2} = \frac{3}{20}\frac{e^2qQ}{h} \qquad \& \qquad \nu''_{5/2} = 2\nu'_{5/2}, \tag{5}$$

respectively. We observed this to be true in our case for both Sb1 and Sb2 sites at room temperature in the pure sample ($x = 0$), $\nu''_{5/2} = 2\nu'_{5/2}$. Therefore, $\eta_{Sb1} = \eta_{Sb2} = 0$, in agreement with [11].

————————

[*] yoey@ucsb.edu, stephendwilson@ucsb.edu
[1] A. A. Coelho, J. Appl. Crystallogr. **51**, 210 (2018).
[2] G. W. Stinton and J. S. Evans, J. Appl. Crystallogr. **40**, 87 (2007).
[3] K. Momma and F. Izumi, J. Appl. Crystallogr. **44**, 1272 (2011).
[4] A. Abragam, *The principles of nuclear magnetism*, 32 (Oxford University Press, 1961).
[5] G. Kresse and J. Furthmüller, Phys. Rev. B **54**, 11169 (1996).
[6] G. Kresse and J. Furthmüller, Comput. Mater. Sci. **6**, 15 (1996).
[7] P. E. Blöchl, Phys. Rev. B **50**, 17953 (1994).
[8] G. Kresse and D. Joubert, Phys. Rev. B **59**, 1758 (1999).
[9] W. Setyawan and S. Curtarolo, Comput. Mater. Sci. **49**, 299 (2010).
[10] A. M. Ganose, A. J. Jackson, and D. O. Scanlon, J. Open Source Softw. **3**, 717 (2018).
[11] J. Luo, Z. Zhao, Y. Zhou, J. Yang, A. Fang, H. Yang, H. Gao, R. Zhou, and G.-q. Zheng, arXiv preprint arXiv:2108.10263 (2021).